

Boundary Integral Formulation of the Cell-by-Cell Model of Cardiac Electrophysiology*

Giacomo Rosilho de Souza^{†1}, Rolf Krause^{‡1,2}, and Simone Pezzuto^{§3,1}

¹Center for Computational Medicine in Cardiology, Euler Institute, Università della Svizzera italiana, via G. Buffi 13, 6900 Lugano, Switzerland

²Faculty of Mathematics and Informatics, FernUni, Schinerstrasse 18, 3900, Brig, Switzerland

³Department of Mathematics, Università di Trento, via Sommarive 14, 38123, Povo (Trento), Italy

February 13, 2023

Abstract

We propose a boundary element method for the accurate solution of the cell-by-cell bidomain model of electrophysiology. The cell-by-cell model, also called Extracellular-Membrane-Intracellular (EMI) model, is a system of reaction-diffusion equations describing the evolution of the electric potential within each domain: intra- and extra-cellular space and the cellular membrane. The system is parabolic but degenerate because the time derivative is only in the membrane domain. In this work, we adopt a boundary-integral formulation for removing the degeneracy in the system and recast it to a parabolic equation on the membrane. The formulation is also numerically advantageous since the number of degrees of freedom is sensibly reduced compared to the original model. Specifically, we prove that the boundary-element discretization of the EMI model is equivalent to a system of ordinary differential equations, and we consider a time discretization based on the multirate explicit stabilized Runge–Kutta method. We numerically show that our scheme converges exponentially in space for the single-cell case. We finally provide several numerical experiments of biological interest.

Keywords. Cell-by-cell model • EMI model • Boundary Element Method • Cardiac Electrophysiology • Gap Junctions

1 Introduction

The human heart is composed of billions of electrically-active myocytes. Altogether, myocytes form a syncytium of cells that enables electrical and mechanical synchronization of the tissue [24]. Cardiac myocytes are excitable cells that can react and transmit electric currents to communicate and coordinate their action. Electrical propagation depends on the conductive properties of the cytoplasm and the extracellular matrix. Cell-to-cell conduction occurs via gap junctions, permeable channel mostly distributed in the myocyte longitudinal direction. Myocyte excitability is due to hundreds of thousands ion channels embedded in the cellular membrane. The overall propagation of the cardiac action potential emerges from a balance of diffusion and transmembrane currents.

Mathematically, cardiac electrophysiology models are systems of reaction-diffusion equations. The reaction term results from transmembrane currents, which are voltage-dependent and regulated through a gating mechanism. Ion channel gating is typically modeled via Hodgkin–Huxley formalism, yielding a possibly large set of ordinary differential equations. The diffusion term captures the spatial coordination

*This work was supported by the European High-Performance Computing Joint Undertaking EuroHPC under grant agreement No 955495 (MICROCARD) co-funded by the Horizon 2020 programme of the European Union (EU) and the Swiss State Secretariat for Education, Research and Innovation.

[†]giacomo.rosilhodesouza@usi.ch

[‡]rolf.krause@usi.ch

[§]simone.pezzuto@unitn.it

of the cardiac tissue. The state-of-the-art model is the bidomain system. Here, the intracellular and extracellular spaces are superimposed and homogenized [30]. Patient-specific organ-scale simulations routinely employ the bidomain model and its monodomain approximation. Despite being physiologically accurate, the bidomain model fails to capture the sub-cellular tissue organization. The cell-by-cell bidomain model accounts for the Extracellular-Membrane-Intracellular (EMI) tissue components as separated (yet coupled) entities [37, 44]. The cell-by-cell model enables a more accurate description of tissue heterogeneities, a key aspect in heart failure and atrial fibrillation [36].

The cell-by-cell model presents several challenges. First, its unusual mathematical formulation showing time dynamics at the boundaries, indeed it presents an ordinary differential equation (ODE) on the transmembrane boundary and a constraint on the gap junctions. Second, in addition to the natural stiffness introduced by the Laplacian, the ionic model introduces stiff nonlinear multiscale dynamics. Third, a full scale heart model would require billions of cells leading to an incredibly large system of equations. Hence, advanced tailored methods must be designed to solve cell-by-cell models.

In the literature, cell-by-cell models have already been solved by means of the finite element or boundary element method. In the finite element community the problem has been tackled by Stinstra and collaborators [41, 39, 42, 40] and more recently by Tveito and collaborators [22, 43, 44, 12] as well. In both cases the cell-by-cell model was employed to study the effects of the cells microscopic structure on macroscopic values as conductive velocity or effective tissue conductivity. Also, the cell-by-cell model was employed to derive the effective parameters for the bidomain model under different microstructural conditions [39, 37, 18]. Bécue, Potse and Coudière [4, 5, 6] compared different gap junctions modelizations and studied existence of solutions in [3]. In the context of the boundary element method the model was solved only for very simple and structured geometries, for instance in [14, 21, 28] for a longitudinal array of non-touching cells, in [45] for two a two-cells model, and more recently, from a theoretical point of view, in [19, 20] it was analyzed for the case of isolated cells.

In this paper we propose a spatial discretization of the cell-by-cell model based on the boundary element method (BEM) and reduce it to a single system of ODEs living only on the transmembrane boundary. The great advantage brought by the BEM is that only boundaries need to be discretized, leading to much smaller systems of equations compared to more traditional methods as finite elements or volumes. We stress that the approach presented here is easily adapted for different gap-junction boundary conditions [44] or unbounded extracellular domains (the “infinite bath” approximation). Also, any spatial discretization method for which Dirichlet-to-Neumann maps can be computed could be employed instead of the BEM. Compared to previous BEM approaches, our methodology is independent from the cells structure and reduces any problem to an ODE on the transmembrane boundary.

This paper is organized as follows. In Section 2 we treat the simple case where only one myocyte cell is present, the purpose of this section is to introduce the needed tools and our approach in a simplified setting. In Section 3 instead we discretize in space the full problem with an arbitrary number of cells, possibly in contact, and reduce it to a system of ODEs. Finally, in Section 4 we present some numerical results.

2 The single-cell problem

The main purpose of this section is to introduce in a simplified setting the boundary integral formulation and the boundary element method (BEM) employed to discretize the full problem, done in Section 3, and as well the approach used to reduce the space discrete problem into a system of ordinary differential equations (ODE).

2.1 Problem formulation

Here we consider the EMI model for a single cell, denoted by the bounded domain $\Omega_1 \subset \mathbb{R}^d$ with $d = 2$, embedded in the extracellular space, denoted by $\Omega_0 \subset \mathbb{R}^d$. See Fig. 1 for a schematic representation of the single-cell problem. Specifically, we require that the intra- and extra-cellular domain do not overlap, that is $\Omega_0 \cap \Omega_1 = \emptyset$, and that they share a common boundary $\Gamma_0 = \bar{\Omega}_0 \cap \bar{\Omega}_1$. The boundary Γ_0 represents the cellular membrane. The membrane model and temporal dynamic of the system, due to capacitative currents, is confined on Γ_0 . We finally assume that Ω_0 is bounded with exterior boundary $\Sigma = \partial\Omega_0 \setminus \Gamma_0$. Also, we define $\Gamma_1 = \partial\Omega_1$ (note that for the single-cell problem $\Gamma_1 = \Gamma_0$). The single-cell problem reads

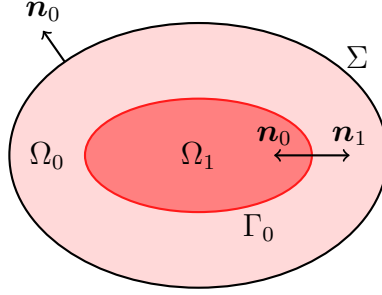


Figure 1: Geometrical setup of problem Eq. (1). The cell and the extra-cellular space are respectively denoted by Ω_1 and Ω_0 . The cellular membrane is Γ_0 .

as follows:

$$\left\{ \begin{array}{ll} -\sigma_1 \Delta u_1 = 0, & \text{in } \Omega_1, \quad (1a) \\ -\sigma_0 \Delta u_0 = 0, & \text{in } \Omega_0, \quad (1b) \\ \sigma_1 \partial_{\mathbf{n}_1} u_1 + \sigma_0 \partial_{\mathbf{n}_0} u_0 = 0, & \text{on } \Gamma_0, \quad (1c) \\ \sigma_0 \partial_{\mathbf{n}_0} u_0 = I_t(V_0, z) = C_m \partial_t V_0 + I_{\text{ion}}(V_0, z), & \text{on } \Gamma_0, \quad (1d) \\ u_1 - u_0 = V_0, & \text{on } \Gamma_0, \quad (1e) \\ \partial_t z = g(V_0, z), & \text{on } \Gamma_0, \quad (1f) \\ \sigma_0 \partial_{\mathbf{n}_0} u_0 = 0, & \text{on } \Sigma, \quad (1g) \end{array} \right. \quad (1h)$$

where $u_0(x, t)$, $u_1(x, t)$, and $V_0(x, t)$ are respectively the intra-cellular, extra-cellular, and transmembrane electric potential, σ_0 and σ_1 are respectively the extra- and intra-cellular electric conductivity, C_m is the membrane capacitance, and \mathbf{n}_i , $i = 0, 1$ is the outwards normal. The ionic model is defined by $z(x, t)$, a vector of gating and concentration variables, its corresponding dynamic in Eq. (1f), and the ionic currents $I_{\text{ion}}(V_0, z)$.

The global well-posedness of the problem (1) in Sobolev spaces has been studied by **(author?)** [29]. The idea of the proof is similar to what we do here, in the sense that the authors recast (1) to an ODE on the interface Γ_0 . The equation involves a pseudo-differential operator not dissimilar to the Dirichlet-Neumann map, as done below in the discrete settings with the operator ψ . We are not aware of similar results for the multi-cell problem.

2.2 Boundary integral formulation

Problem in Eq. (1) has already been tackled and carefully analyzed by **(author?)** [20], where the BEM with a Galerkin approach was employed. Here, we derive a boundary integral formulation of the unicellular problem Eq. (1) in terms of trace operators and Poincaré–Steklov operators.

Let γ_t^1 be the trace operator and γ_n^1 the conormal derivative on the boundary Γ_1 . More specifically, we introduce the operators as follows:

$$\begin{aligned} \gamma_t^1: H^1(\Omega_1) &\rightarrow H^{1/2}(\Gamma_1), & \gamma_t^1 u_1(\mathbf{x}) &= \lim_{\Omega_1 \ni \mathbf{y} \rightarrow \mathbf{x} \in \Gamma_1} u_1(\mathbf{y}), \\ \gamma_n^1: H^1(\Omega_1) &\rightarrow H^{-1/2}(\Gamma_1), & \gamma_n^1 u_1(\mathbf{x}) &= \lim_{\Omega_1 \ni \mathbf{y} \rightarrow \mathbf{x} \in \Gamma_1} \langle \nabla u_1(\mathbf{y}), \mathbf{n}_1 \rangle, \end{aligned} \quad (2)$$

where the limits on the right must hold for smooth enough u_1 . Let $G(\mathbf{x}, \mathbf{y})$ be the fundamental solution of the Laplacian in \mathbb{R}^d , the Green representation formula for u_1 satisfying Eq. (1a) implies that

$$u_1(\mathbf{x}) = \int_{\Gamma_1} \gamma_{t,\mathbf{y}}^1 G(\mathbf{x}, \mathbf{y}) \gamma_n^1 u_1(\mathbf{y}) \, ds_{\mathbf{y}} - \int_{\Gamma_1} \gamma_{n,\mathbf{y}}^1 G(\mathbf{x}, \mathbf{y}) \gamma_t^1 u_1(\mathbf{y}) \, ds_{\mathbf{y}}, \quad \mathbf{x} \in \Omega_1 \quad (3)$$

where \mathbf{y} in $\gamma_{t,\mathbf{y}}^1, \gamma_{n,\mathbf{y}}^1$ means that the operators are applied to the second variable of $G(\mathbf{x}, \mathbf{y})$. Taking the trace γ_t^1 of Eq. (3) we obtain

$$\gamma_t^1 u_1 = \mathcal{V}_1 \gamma_n^1 u_1 - (\mathcal{K}_1 - \frac{1}{2}I) \gamma_t^1 u_1, \quad (4)$$

where I is the identity operator, \mathcal{V}_1 and \mathcal{K}_1 are the single and double layer operators defined by

$$\begin{aligned}\mathcal{V}_1: H^{-1/2}(\Gamma_1) &\rightarrow H^{1/2}(\Gamma_1), & \mathcal{V}_1\rho(\mathbf{x}) &= \int_{\Gamma_1} \gamma_{t,\mathbf{y}}^1 G(\mathbf{x}, \mathbf{y}) \rho(\mathbf{y}) \, ds_{\mathbf{y}}, & \mathbf{x} &\in \Gamma_1, \\ \mathcal{K}_1: H^{1/2}(\Gamma_1) &\rightarrow H^{1/2}(\Gamma_1), & \mathcal{K}_1\rho(\mathbf{x}) &= \int_{\Gamma_1} \gamma_{n,\mathbf{y}}^1 G(\mathbf{x}, \mathbf{y}) \rho(\mathbf{y}) \, ds_{\mathbf{y}}, & \mathbf{x} &\in \Gamma_1,\end{aligned}\tag{5}$$

and the term $\frac{1}{2}I$ in Eq. (4) comes from the jump of the double layer potential as $\Omega_1 \ni \mathbf{x} \rightarrow \mathbf{y} \in \Gamma_1$. Problem Eq. (4) can be rewritten as

$$\mathcal{V}_1\gamma_n^1 u_1 = (\mathcal{K}_1 + \frac{1}{2}I)\gamma_t^1 u_1,\tag{6}$$

or employing the Poincaré–Steklov operator (Dirichlet-to-Neumann map):

$$\mathcal{P}_1: H^{1/2}(\Gamma_1) \rightarrow H^{-1/2}(\Gamma_1), \quad \mathcal{P}_1 := \mathcal{V}_1^{-1}(\mathcal{K}_1 + \frac{1}{2}I),\tag{7}$$

then Eq. (6) becomes

$$\gamma_n^1 u_1 = \mathcal{P}_1 \gamma_t^1 u_1.\tag{8}$$

The Poincaré–Steklov operator \mathcal{P}_1 in Eq. (7) is known to be symmetric [35, Section 3.7]. Now, let $\gamma_t^0 u_0$, $\gamma_n^0 u_0$ be the trace and conormal derivative of u_0 on $\Gamma_0 = \Gamma_1$, respectively. In order to derive a Dirichlet-to-Neumann map $\mathcal{P}_0: H^{1/2}(\Gamma_0) \rightarrow H^{-1/2}(\Gamma_0)$ in Ω_0 , hence

$$\gamma_n^0 u_0 = \mathcal{P}_0 \gamma_t^0 u_0,\tag{9}$$

we need to take into account the boundary condition (1g) on the external boundary Σ of Ω_0 . In order to alleviate the presentation we postpone the derivation of \mathcal{P}_0 to A. However, we would like to note that \mathcal{P}_0 remains symmetric.

Due to the Green representation formula, Eqs. (1a) and (1b) can be dropped from Eq. (1). Also, Eq. (1g) is encoded into the definition of \mathcal{P}_0 (see A). Finally, the boundary integral formulation of Eq. (1) is

$$\begin{cases} \sigma_1 \mathcal{P}_1 \gamma_t^1 u_1 + \sigma_0 \mathcal{P}_0 \gamma_t^0 u_0 = 0, & (10a) \\ \gamma_t^1 u_1 - \gamma_t^0 u_0 = V_0, & (10b) \\ \sigma_0 \mathcal{P}_0 \gamma_t^0 u_0 = I_t(V_0, z), & (10c) \\ \partial_t z = g(V_0, z). & (10d) \end{cases}$$

2.3 Spatial discretization of the unicellular problem

We adopt the collocation BEM as spatial discretization scheme. Boundary element methods have less degrees of freedom than other standard techniques, while the collocation approach yields lower dimensional boundary integrals than the variational method and hence faster computations. For extensive presentations on the BEM we refer to [26, 35, 38].

We place M collocation points \mathbf{x}_j , $j = 1, \dots, M$, on Γ_1 in a counterclockwise order. Then we compute a smooth parametrization $\gamma_{\Gamma_1}: [0, 1) \rightarrow \Gamma_1$ satisfying

$$\gamma_{\Gamma_1}(t_j) = \mathbf{x}_j \quad j = 1, \dots, M,\tag{11}$$

where $\{t_j\}_{j=1}^M \subset [0, 1)$ is an increasing sequence. (The parametrization γ_{Γ_1} is computed with Fourier interpolation. For the unicellular problem, we could define $\gamma_{\Gamma_1}(t)$ first and then set \mathbf{x}_j as in Eq. (11). However, this is not possible for the multi cell problems.) Finally, we represent $\gamma_t^1 u_1$, $\gamma_n^1 u_1$ as

$$\gamma_t^1 u_1(\gamma_{\Gamma_1}(t)) = \sum_{j=1}^M u_1^j L_j(t), \quad \gamma_n^1 u_1(\gamma_{\Gamma_1}(t)) = \sum_{j=1}^M \tilde{u}_1^j L_j(t),\tag{12}$$

where $L_j(t)$ are trigonometric Lagrange polynomials satisfying $L_j(t_k) = \delta_{jk}$ for $j, k = 1, \dots, M$. Instead of Eq. (6) we solve the weaker form

$$\mathcal{V}_1 \gamma_n^1 u_1(\mathbf{x}_k) = (\mathcal{K}_1 + \frac{1}{2}I)\gamma_t^1 u_1(\mathbf{x}_k), \quad k = 1, \dots, M,\tag{13}$$

with $\mathbf{x}_k = \gamma_{\Gamma_1}(t_k)$, which is equivalent to

$$\sum_{j=1}^M \tilde{u}_1^j \mathcal{V}_1 L_j(\gamma_{\Gamma_1}^{-1}(\mathbf{x}_k)) = \sum_{j=1}^M u_1^j (\mathcal{K}_1 + \frac{1}{2}I) L_j(\gamma_{\Gamma_1}^{-1}(\mathbf{x}_k)), \quad k = 1, \dots, M, \quad (14)$$

and hence the linear system

$$V_1 \tilde{\mathbf{u}}_1 = (K_1 + \frac{1}{2}I) \mathbf{u}_1, \quad (15)$$

with $\mathbf{u}_1, \tilde{\mathbf{u}}_1$ the vectors of coefficients u_1^j, \tilde{u}_1^j , respectively, and

$$(V_1)_{kj} := \mathcal{V}_1(L_j \circ \gamma_{\Gamma_1}^{-1})(\mathbf{x}_k) = \int_{\Gamma_1} \gamma_{t,\mathbf{y}}^1 G(\mathbf{x}_k, \mathbf{y}) L_j(\gamma_{\Gamma_1}^{-1}(\mathbf{y})) ds_{\mathbf{y}} = \int_0^1 \gamma_{t,\mathbf{y}}^1 G(\mathbf{x}_k, \gamma_{\Gamma_1}(t)) L_j(t) \|\gamma'_{\Gamma_1}(t)\| dt,$$

$$(K_1)_{kj} := \mathcal{K}_1(L_j \circ \gamma_{\Gamma_1}^{-1})(\mathbf{x}_k) = \int_{\Gamma_1} \gamma_{n,\mathbf{y}}^1 G(\mathbf{x}_k, \mathbf{y}) L_j(\gamma_{\Gamma_1}^{-1}(\mathbf{y})) ds_{\mathbf{y}} = \int_0^1 \gamma_{n,\mathbf{y}}^1 G(\mathbf{x}_k, \gamma_{\Gamma_1}(t)) L_j(t) \|\gamma'_{\Gamma_1}(t)\| dt.$$

The matrix coefficients $(V_1)_{kj}, (K_1)_{kj}$ must be computed with special care due to the singularities in the fundamental solution $G(\mathbf{x}, \mathbf{y})$ and its derivatives as $\gamma_{\Gamma_1}(t) \rightarrow \mathbf{x}_k$, we refer to [16, 26] for the details.

Note that \mathbf{u}_1 and $\tilde{\mathbf{u}}_1$ are the vectors of coordinates of $\gamma_t^1 u_1$ and $\gamma_n^1 u_1$, respectively, and that from Eq. (15) follow the discrete version of Eq. (8)

$$\tilde{\mathbf{u}}_1 = P_1 \mathbf{u}_1, \quad P_1 := (V_1)^{-1} (K_1 + \frac{1}{2}I), \quad (16)$$

where P_1 is the discrete Poincaré–Steklov operator (Dirichlet-to-Neumann map) in Ω_1 . Similarly, in A we derive the discrete version of Eq. (9) and obtain

$$\tilde{\mathbf{u}}_0 = P_0 \mathbf{u}_0, \quad (17)$$

with \mathbf{u}_0 and $\tilde{\mathbf{u}}_0$ the vectors of coordinates of $\gamma_t^0 u_0$ and $\gamma_n^0 u_0$, respectively.

Finally, the space discretization of boundary integral formulation Eq. (10) is

$$\begin{cases} \sigma_1 P_1 \mathbf{u}_1 + \sigma_0 P_0 \mathbf{u}_0 = 0, & (18a) \\ \mathbf{u}_1 - \mathbf{u}_0 = \mathbf{V}_0, & (18b) \\ \sigma_0 P_0 \mathbf{u}_0 = I_t(\mathbf{V}_0, \mathbf{z}), & (18c) \\ \mathbf{z}' = g(\mathbf{V}_0, \mathbf{z}), & (18d) \end{cases}$$

where $\mathbf{V}_0(t) \in \mathbb{R}^M$ is the vector whose coefficients represent $V_0(\mathbf{x}_j, t)$ and analogously for \mathbf{z} . The right-hand sides I_t and g are applied to \mathbf{V}_0, \mathbf{z} component wise. If needed, the solution u_1 satisfying Eq. (1a) is approximated via the Green identity Eq. (3) and Eq. (12), Eq. (16). We proceed similarly for u_0 .

2.4 The Lagrange multipliers approach for the unicellular problem

Now we solve Eq. (18) and to do so we employ the Lagrange multiplier method. We adopted this technique mainly for pedagogical reasons in regard of what will be presented in Section 3, since for the unicellular problem Eq. (1) a more direct approach could be used.

In the remaining of this section we construct the linear map

$$\psi : \mathbb{R}^M \rightarrow \mathbb{R}^M, \quad \psi(\mathbf{V}_0) = \sigma_0 P_0 \mathbf{u}_0, \quad (19)$$

where \mathbf{u}_0 satisfies Eqs. (18a) and (18b) (behind the scenes \mathbf{u}_1 is computed as well, but it is not needed as output of ψ). Inserting Eq. (19) and $I_t(\mathbf{V}_0, \mathbf{z}) = C_m \mathbf{V}_0' + I_{\text{ion}}(\mathbf{V}_0, \mathbf{z})$ in Eqs. (18c) and (18d) the problem reduces to the ODE

$$\begin{cases} C_m \mathbf{V}_0' + I_{\text{ion}}(\mathbf{V}_0, \mathbf{z}) = \psi(\mathbf{V}_0), & (20a) \\ \mathbf{z}' = g(\mathbf{V}_0, \mathbf{z}), & (20b) \end{cases}$$

which can be integrated by any suitable time marching scheme. Eq. (20) has the same structure as the one derived in [20], where a BEM for the cell-by-cell model without gap junctions is derived.

Theorem 2.1 is the unicellular version of the more general Theorem 3.1 below, which in turn takes inspiration from the work in [27]. We also remark that the Theorem is independent on the spatial discretization. For instance, a finite element discretization may be recast to Eq. (18) by static condensation, that it by explicitly computing the discrete Poincaré–Steklov operator.

Theorem 2.1. *The linear map ψ from Eq. (19) satisfies $\psi(\mathbf{V}_0) = \boldsymbol{\lambda}$, with $\boldsymbol{\lambda} \in \mathbb{R}^M$ and $\beta_1 \in \mathbb{R}$ solution to*

$$\begin{pmatrix} F & G \\ G^\top & 0 \end{pmatrix} \begin{pmatrix} \boldsymbol{\lambda} \\ \beta_1 \end{pmatrix} = \begin{pmatrix} \mathbf{V}_0 \\ 0 \end{pmatrix}. \quad (21)$$

The matrices $F \in \mathbb{R}^{M \times M}$, $G \in \mathbb{R}^M$ are defined by

$$F = -(\sigma_1^{-1}(P_1^+)^{-1} + \sigma_0^{-1}(P_0^+)^{-1}), \quad G = \mathbf{e}, \quad (22)$$

$\mathbf{e} \in \mathbb{R}^M$ is the vector of ones and

$$P_0^+ = P_0 + \alpha_0 \mathbf{e} \mathbf{e}^\top, \quad P_1^+ = P_1 + \alpha_1 \mathbf{e} \mathbf{e}^\top, \quad (23)$$

with $\alpha_0, \alpha_1 > 0$. If needed, $\mathbf{u}_1, \mathbf{u}_0$ are computed with

$$\mathbf{u}_0 = \sigma_0^{-1}(P_0^+)^{-1} \boldsymbol{\lambda}, \quad \mathbf{u}_1 = -\sigma_1^{-1}(P_1^+)^{-1} \boldsymbol{\lambda} + \beta_1 \mathbf{e}. \quad (24)$$

Hence, when solving the ODE system Eq. (20) with a time integration scheme, every time that $\psi(\mathbf{V}_0)$ needs to be evaluated system Eq. (21) is solved and $\psi(\mathbf{V}_0) = \boldsymbol{\lambda}$ is inserted in Eq. (20).

Proof of Theorem 2.1. Vectors $\mathbf{u}_1, \mathbf{u}_0$ are solutions to the smaller system in Eqs. (18a) and (18b). Since P_0, P_1 are symmetric, $\mathbf{u}_1, \mathbf{u}_0$ are also solution to the constrained minimization problem

$$\min_{\mathbf{u}_1, \mathbf{u}_0} \frac{\sigma_0}{2} \langle P_0 \mathbf{u}_0, \mathbf{u}_0 \rangle + \frac{\sigma_1}{2} \langle P_1 \mathbf{u}_1, \mathbf{u}_1 \rangle \quad \text{with} \quad \mathbf{u}_1 - \mathbf{u}_0 = \mathbf{V}_0, \quad (25)$$

where $\langle \cdot, \cdot \rangle$ is the Euclidean inner product in \mathbb{R}^M . Let

$$\mathcal{L}(\mathbf{u}_0, \mathbf{u}_1, \boldsymbol{\lambda}) = \frac{\sigma_0}{2} \langle P_0 \mathbf{u}_0, \mathbf{u}_0 \rangle + \frac{\sigma_1}{2} \langle P_1 \mathbf{u}_1, \mathbf{u}_1 \rangle + \langle \mathbf{u}_1 - \mathbf{u}_0 - \mathbf{V}_0, \boldsymbol{\lambda} \rangle \quad (26)$$

be the Lagrangian function, imposing $\nabla \mathcal{L}(\mathbf{u}_0, \mathbf{u}_1, \boldsymbol{\lambda}) = \mathbf{0}$ yields

$$\sigma_0 P_0 \mathbf{u}_0 - \boldsymbol{\lambda} = \mathbf{0}, \quad \sigma_1 P_1 \mathbf{u}_1 + \boldsymbol{\lambda} = \mathbf{0}, \quad \mathbf{u}_1 - \mathbf{u}_0 = \mathbf{V}_0. \quad (27)$$

Note that $P_0 \mathbf{e} = \mathbf{0}$, with $\mathbf{e} \in \mathbb{R}^M$ a vector of ones, thus P_0 is singular and the first equation of (27) $\sigma_0 P_0 \mathbf{u}_0 = \boldsymbol{\lambda}$ has a solution only if

$$\langle \boldsymbol{\lambda}, \mathbf{e} \rangle = 0. \quad (28)$$

Let

$$P_0^+ = P_0 + \alpha_0 \mathbf{e} \mathbf{e}^\top \quad (29)$$

with $\alpha_0 > 0$, then P_0^+ is invertible and it can be verified that if Eq. (28) holds then

$$\mathbf{u}_0 = \sigma_0^{-1}(P_0^+)^{-1} \boldsymbol{\lambda} + \beta_0 \mathbf{e}, \quad \beta_0 \in \mathbb{R}, \quad (30)$$

is solution to $\sigma_0 P_0 \mathbf{u}_0 = \boldsymbol{\lambda}$. Similarly,

$$\mathbf{u}_1 = -\sigma_1^{-1}(P_1^+)^{-1} \boldsymbol{\lambda} + \beta_1 \mathbf{e}, \quad \beta_1 \in \mathbb{R}, \quad (31)$$

is solution to $\sigma_1 P_1 \mathbf{u}_1 = -\boldsymbol{\lambda}$, with P_1^+ defined analogously to P_0^+ . Note that if $\mathbf{u}_0, \mathbf{u}_1$ are solutions to Eqs. (18a) and (18b) then $\mathbf{u}_0 + C\mathbf{e}, \mathbf{u}_1 + C\mathbf{e}$ are solutions for all $C \in \mathbb{R}$. We choose to fix such free constant by setting $\beta_0 = 0$, which implies $\sum_{j=1}^M u_0^j = 0$. The last equation of Eq. (27) yields

$$\mathbf{V}_0 = \mathbf{u}_1 - \mathbf{u}_0 = -(\sigma_1^{-1}(P_1^+)^{-1} + \sigma_0^{-1}(P_0^+)^{-1}) \boldsymbol{\lambda} + \beta_1 \mathbf{e} = F \boldsymbol{\lambda} + G \beta_1, \quad (32)$$

with matrices F, G as in Eq. (22). Together with Eq. (28) it yields system Eq. (21). \square

Remark 2.2. *Note that the content of this section is readily adapted to a problem Eq. (1) with unbounded domain Ω_0 , hence without boundary condition (1g). In that case, P_0 is derived analogously to P_1 . However, P_0 would be non singular hence in Theorem 2.1 we consider Eq. (29) with $\alpha_0 = 0$. Condition Eq. (28) is still required for the existence of a solution to $\sigma_1 P_1 \mathbf{u}_1 = -\boldsymbol{\lambda}$.*

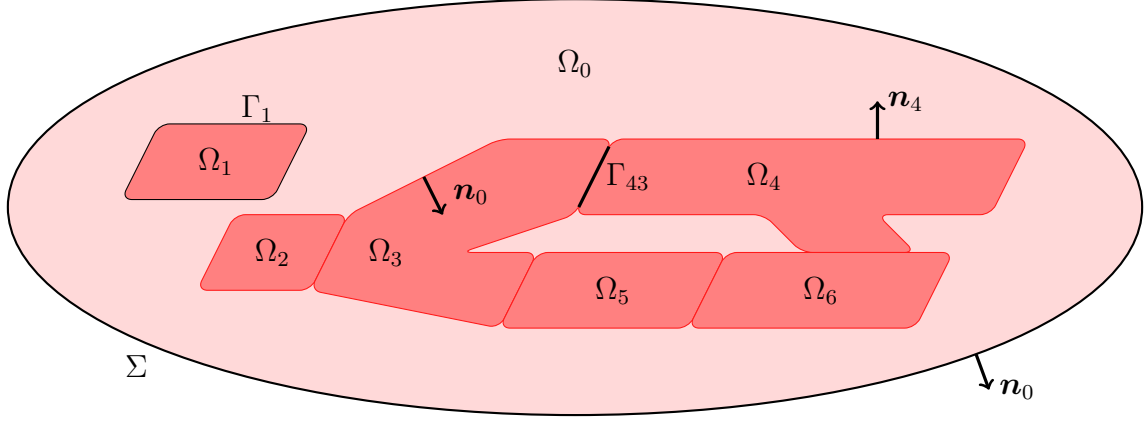


Figure 2: Illustration of problem Eq. (33).

3 Discretization of the full cell-by-cell model

We introduce here the general cell-by-cell model. We consider an extracellular domain $\Omega_0 \subset \mathbb{R}^d$, $d \geq 2$, an intracellular domain $\Omega_I \subset \mathbb{R}^d$, and an interface domain $\Gamma_0 = \Omega_0 \cap \Omega_I$. (See Figure 2 for a graphical illustration of the model.) We suppose that Ω_I and Ω_0 are disjoint and we denote by Ω the whole tissue, $\Omega = \Omega_I \cup \Omega_0 \cup \Gamma_0$. The domain Ω is always assumed connected and bounded, with $\Sigma = \partial\Omega$. For the sake of simplicity, $\partial\Omega_0 \setminus \Gamma_0 = \Sigma$ and $\partial\Omega_I = \Gamma_0$, that is the exterior boundary of Ω always corresponds to the extracellular matrix. Next, the intracellular space is described by the union of disjoint cells, denoted by Ω_i , $i = 1, \dots, N$. (Conveniently, Ω_i for $i = 0$ corresponds to the extracellular space.) Thus, $\Omega_I = \bigcup_{i=1}^N \Omega_i$. We denote $\Gamma_i = \partial\Omega_i$, $i = 1, \dots, N$. The cell-to-cell interconnections are denoted by $\Gamma_{ij} = \Gamma_i \cap \Gamma_j$, $0 \leq j < i \leq N$. Note that the boundary of each cell is either in contact with another cell or with the extracellular space. The cell-by-cell model reads as follows:

$$\left\{ \begin{array}{ll} -\sigma_i \Delta u_i = 0, & \text{in } \Omega_i, i = 0, \dots, N, \quad (33a) \\ u_i - u_0 = V_{i0}, & \text{on } \Gamma_{i0} \text{ for } 1 \leq i \leq N, \quad (33b) \\ -\sigma_i \partial_{\mathbf{n}_i} u_i = C_m \partial_t V_{i0} + I_{\text{ion}}(V_{i0}, z_i), & \text{on } \Gamma_{i0} \text{ for } 1 \leq i \leq N, \quad (33c) \\ -\sigma_0 \partial_{\mathbf{n}_0} u_0 = -C_m \partial_t V_{i0} - I_{\text{ion}}(V_{i0}, z_i), & \text{on } \Gamma_{i0} \text{ for } 1 \leq i \leq N, \quad (33d) \\ \partial_t z_i = g(V_{i0}, z_i), & \text{on } \Gamma_0, \quad (33e) \\ -\sigma_i \partial_{\mathbf{n}_i} u_i = \kappa(u_i - u_j), & \text{on } \Gamma_{ij} \text{ for } 1 \leq j < i \leq N, \quad (33f) \\ -\sigma_0 \partial_{\mathbf{n}_0} u_0 = 0, & \text{on } \Sigma. \quad (33g) \end{array} \right. \quad (33h)$$

The constant conductivities are σ_i , $i = 0, \dots, N$. The gap junctions (intercellular connections) are represented by Γ_{ij} for $1 \leq j < i \leq N$, with permeability κ . The normals \mathbf{n}_i point outwards to Ω_i . The intracellular potentials are u_i for $i = 1, \dots, N$, the extracellular potential is u_0 and V_{i0} is the transmembrane potential on Γ_{i0} . The membrane electric capacitance is C_m and I_{ion} represents the sum of ionic currents. The transmembrane potential V_{i0} is regulated by the ionic currents, which in turn depend on ionic concentrations and their transmembrane fluxes through ion channels, which are governed by gating variables. Ion concentrations and gating variables are represented by z_i and the pair I_{ion}, g describe the membrane ionic model. Several ionic models exist and they typically consist of few to hundreds of equations. We remark that there is no restriction in the system (33) for having different ionic models on each cell.

Model Eq. (33) is a slight simplification of a more detailed model by (author?) [44], where the dynamics at the gap junctions is time dependent and nonlinear in $u_i - u_j$. The simplification adopted here follows from linearization and an equilibrium assumption. This procedure leads to a less computationally intensive model. Solving the complete model and compare the results is subject of a future work.

In this section we adapt the techniques used in Section 2 to the full problem Eq. (33). First, in Section 3.1, we perform the spatial discretization of the cell-by-cell model, obtaining a differential algebraic equation. Then, in Section 3.2, we reduce the problem to a system of ordinary differential equations on the transmembrane boundary.

We start rewriting Eq. (33) as follows. Let $V_{ij} = u_i - u_j$ be the difference of potential defined on the gap junctions Γ_{ij} for $1 \leq j < i \leq N$. Please note that we consider Γ_{ij} with $j < i$ only, this is to avoid any confusion regarding the sign of u_i and u_j in the definition of V_{ij} . Let $\Gamma_g = \cup_{1 \leq j < i \leq N} \Gamma_{ij}$ be the union of all gap junctions, Γ_0 is the transmembrane boundary and $\Gamma = \Gamma_0 \cup \Gamma_g$ the union of all internal boundaries. We define V on Γ by $V|_{\Gamma_{ij}} = V_{ij}$. This yields Eq. (34c) instead of Eq. (33b). Condition (33d) yields Eq. (34e), while summing Eqs. (33c) and (33d) we obtain Eq. (34b) for $j = 0$. Summing Eq. (33f) inverting the roles of i, j yields Eq. (34b) for $j \geq 1$, while taking the difference gives Eq. (34d).

$$\left\{ \begin{array}{ll} -\sigma_i \Delta u_i = 0, & \text{in } \Omega_i \text{ for } i = 0, \dots, N, \\ \sigma_i \partial_{\mathbf{n}_i} u_i + \sigma_j \partial_{\mathbf{n}_j} u_j = 0, & \text{on } \Gamma_{ij} \text{ for } 0 \leq j < i \leq N, \\ u_i - u_j = V, & \text{on } \Gamma_{ij} \text{ for } 0 \leq j < i \leq N, \\ \sigma_j \partial_{\mathbf{n}_j} u_j - \sigma_i \partial_{\mathbf{n}_i} u_i = 2\kappa V, & \text{on } \Gamma_{ij} \text{ for } 1 \leq j < i \leq N, \\ \sigma_0 \partial_{\mathbf{n}_0} u_0 = I_t(V, z), & \text{on } \Gamma_0, \\ \partial_t z = g(V, z), & \text{on } \Gamma_0. \\ \sigma_0 \partial_{\mathbf{n}_0} u_0 = 0, & \text{on } \Sigma. \end{array} \right. \quad \begin{array}{l} (34a) \\ (34b) \\ (34c) \\ (34d) \\ (34e) \\ (34f) \\ (34g) \end{array}$$

Model Eq. (34) is equivalent to Eq. (33), however it is written in a more ‘‘symmetric’’ manner.

3.1 Spatial discretization of the cell-by-cell model

We discretize all boundary segments Γ_{ij} with M_{ij} collocation points $\mathbf{x}_{ij}^k \in \overset{\circ}{\Gamma}_{ij}$, for $k = 1, \dots, M_{ij}$ and $0 \leq j < i \leq N$. Let M_i be the number of discretization points lying on boundary Γ_i , $i = 0, \dots, N$. The total number of collocation points on $\Gamma = \cup_{i=0}^N \Gamma_i$ is $M = \sum_{0 \leq j < i \leq N} M_{ij} = \frac{1}{2} \sum_{i=0}^N M_i$. We denote \mathbf{x}^l , $l = 1, \dots, M$, the global collocations points on Γ and by \mathbf{x}_i^k , $k = 1, \dots, M_i$, the local collocation points on Γ_i . Note that every \mathbf{x}^l lies on some Γ_{ij} , hence there are $\mathbf{x}_{ij}^{k_1}, \mathbf{x}_i^{k_2}, \mathbf{x}_j^{k_3}$ satisfying $\mathbf{x}^l = \mathbf{x}_{ij}^{k_1} = \mathbf{x}_i^{k_2} = \mathbf{x}_j^{k_3}$.

Let $A_i \in \mathbb{R}^{M_i \times M}$ be the boolean connectivity matrix mapping a vector $\mathbf{v} \in \mathbb{R}^M$ of global nodal values on Γ to the vector $\mathbf{v}_i \in \mathbb{R}^{M_i}$ of local nodal values on Γ_i . Every line of A_i has exactly one non zero element: $(A_i)_{kl} = 1$ for k, l such that $\mathbf{x}^l = \mathbf{x}_i^k$. Note that A_i^\top maps local to global degrees of freedom. We also define $B_i \in \mathbb{R}^{M_i \times M}$ having the same sparsity pattern as A_i . Let $(B_i)_{kl}$ be the only non zero element in the k -th line, hence $\mathbf{x}^l = \mathbf{x}_i^k$. If $\mathbf{x}^l \in \Gamma_{ij}$ with $j < i$ then $(B_i)_{kl} = 1$, else $(B_i)_{kl} = -1$.

Let $P_i \in \mathbb{R}^{M_i \times M_i}$ be the discrete Poincaré–Steklov operator on each domain Ω_i and $\mathbf{u}_i \in \mathbb{R}^{M_i}$ the vector of coordinates representing $\gamma_0^i u_i$. The vector of coordinates $\mathbf{V} \in \mathbb{R}^M$ represents V and $\mathbf{V}_0 = A_0 \mathbf{V}$ represents $V|_{\Gamma_0}$. The spatial discretization of Eqs. (34b) and (34c) is given by

$$\sum_{i=0}^N \sigma_i A_i^\top P_i \mathbf{u}_i = \mathbf{0}, \quad \sum_{i=0}^N B_i^\top \mathbf{u}_i = \mathbf{V}. \quad (35)$$

Recall that A_0 is the connectivity matrix mapping a global vector $\mathbf{v} \in \mathbb{R}^M$ to a local vector $\mathbf{v}_0 \in \mathbb{R}^{M_0}$ on the transmembrane boundary Γ_0 . Let $M_g = M - M_0$ be the number of points on the gap junctions Γ_g and $A_g \in \mathbb{R}^{M_g \times M}$ the matrix mapping a global vector to a local vector $\mathbf{v}_g \in \mathbb{R}^{M_g}$ on Γ_g . The spatial discretization of Eqs. (34d) and (34e) is

$$\sigma_0 P_0 \mathbf{u}_0 = I_t(A_0 \mathbf{V}, \mathbf{z}), \quad \sum_{i=1}^N \sigma_i A_g B_i^\top P_i \mathbf{u}_i = -2\kappa A_g \mathbf{V}. \quad (36)$$

As in Section 2, conditions Eqs. (34a) and (34g) are automatically satisfied by the Green representation formula (3) and the definition of the Poincaré–Steklov operator P_0 on Ω_0 . Finally, the spatial discretization of Eq. (34f) is

$$\mathbf{z}' = g(A_0 \mathbf{V}, \mathbf{z}). \quad (37)$$

Hence, the spatial discretization of Eq. (34) is given by Eqs. (35) to (37).

3.2 Reduction to an ordinary differential equation

In this section we transform the space discretization Eqs. (35) to (37) into an ordinary differential equation. First, similarly to Section 2.4, we search for linear maps

$$\psi_i : \mathbb{R}^M \rightarrow \mathbb{R}^{M_i}, \quad \psi_i(\mathbf{V}) = \sigma_i P_i \mathbf{u}_i, \quad i = 0, \dots, N, \quad (38)$$

where the \mathbf{u}_i satisfy Eq. (35). With the help of these maps we can dispose of Eq. (35) by inserting Eq. (38) into Eq. (36) and obtain the system of equations

$$\psi_0(\mathbf{V}) = I_t(A_0\mathbf{V}, \mathbf{z}) = C_m A_0 \mathbf{V}' + I_{\text{ion}}(A_0\mathbf{V}, \mathbf{z}), \quad \sum_{i=1}^N A_g B_i^\top \psi_i(\mathbf{V}) = -2\kappa A_g \mathbf{V}. \quad (39)$$

However, Eq. (39) is a differential algebraic equation (DAE), which requires more involved time marching schemes than a simple ODE. Therefore, departing from the definition of the maps ψ_i given in Theorem 3.1, in Theorem 3.2 we derive a new map which takes into account also the algebraic condition (second equality in Eq. (39)). This new map will allow us to derive an ODE instead of a DAE.

We start with the theorem below, where we compute the maps ψ_i of Eq. (38). The procedure adopted here is inspired from [27], where a domain decomposition technique for the BEM is presented.

Theorem 3.1. *The linear maps ψ_i from Eq. (38) satisfy*

$$\psi_i(\mathbf{V}) = -B_i \boldsymbol{\lambda}, \quad (40)$$

with $\boldsymbol{\lambda} \in \mathbb{R}^M$ and $\boldsymbol{\beta} \in \mathbb{R}^N$ solution to

$$\begin{pmatrix} F & G \\ G^\top & 0 \end{pmatrix} \begin{pmatrix} \boldsymbol{\lambda} \\ \boldsymbol{\beta} \end{pmatrix} = \begin{pmatrix} \mathbf{V} \\ \mathbf{0} \end{pmatrix}. \quad (41)$$

The matrices $F \in \mathbb{R}^{M \times M}$, $G \in \mathbb{R}^{M \times N}$ are defined by

$$F = -\sum_{i=0}^N \sigma_i^{-1} B_i^\top (P_i^+)^{-1} B_i, \quad G = (B_1^\top \mathbf{e}_1, \dots, B_N^\top \mathbf{e}_N), \quad (42)$$

$\mathbf{e}_i \in \mathbb{R}^{M_i}$ is the vector of ones and

$$P_i^+ = P_i + \alpha_i \mathbf{e}_i \mathbf{e}_i^\top, \quad (43)$$

with $\alpha_i > 0$, $i = 0, \dots, N$. If needed, \mathbf{u}_i for $i = 0, \dots, N$ is computed with

$$\mathbf{u}_i = -\sigma_i^{-1} (P_i^+)^{-1} B_i \boldsymbol{\lambda} + \beta_i \mathbf{e}_i, \quad (44)$$

where $\boldsymbol{\beta} = (\beta_1, \dots, \beta_N)^\top$ and $\beta_0 = 0$.

Proof. As in Section 2.4 we notice that instead of solving Eq. (35) we can solve a constrained minimization problem with Lagrangian function

$$\mathcal{L}(\mathbf{u}_0, \dots, \mathbf{u}_N, \boldsymbol{\lambda}) = \sum_{i=0}^N \frac{\sigma_i}{2} \langle P_i \mathbf{u}_i, \mathbf{u}_i \rangle + \sum_{i=0}^N \langle B_i^\top \mathbf{u}_i, \boldsymbol{\lambda} \rangle - \langle \mathbf{V}, \boldsymbol{\lambda} \rangle. \quad (45)$$

Indeed,

$$\nabla_{\boldsymbol{\lambda}} \mathcal{L}(\mathbf{u}_0, \dots, \mathbf{u}_N, \boldsymbol{\lambda}) = \sum_{i=0}^N B_i^\top \mathbf{u}_i - \mathbf{V} = \mathbf{0} \quad (46)$$

is equivalent to the second equality in Eq. (35). The first equality in Eq. (35) follows from

$$\nabla_{\mathbf{u}_i} \mathcal{L}(\mathbf{u}_0, \dots, \mathbf{u}_N, \boldsymbol{\lambda}) = \sigma_i P_i \mathbf{u}_i + B_i \boldsymbol{\lambda} = \mathbf{0} \quad (47)$$

and

$$\mathbf{0} = \sum_{i=0}^N A_i^\top \nabla_{\mathbf{u}_i} \mathcal{L}(\mathbf{u}_0, \dots, \mathbf{u}_N, \boldsymbol{\lambda}) = \sum_{i=0}^N \sigma_i A_i^\top P_i \mathbf{u}_i + A_i^\top B_i \boldsymbol{\lambda} = \sum_{i=0}^N \sigma_i A_i^\top P_i \mathbf{u}_i, \quad (48)$$

where we used $\sum_{i=0}^N A_i^\top B_i = 0$ (for every 1 there is a -1).

Let us solve Eq. (47). We denote $\mathbf{e}_i \in \mathbb{R}^{M_i}$ the vector of ones, imposing

$$\langle B_i \boldsymbol{\lambda}, \mathbf{e}_i \rangle = 0, \quad i = 0, \dots, N, \quad (49)$$

a solution \mathbf{u}_i to Eq. (47) exists and is given by

$$\mathbf{u}_i = -\sigma_i^{-1} (P_i^+)^{-1} B_i \boldsymbol{\lambda} + \beta_i \mathbf{e}_i, \quad \text{with } P_i^+ = P_i + \alpha_i \mathbf{e}_i \mathbf{e}_i^\top, \quad (50)$$

$\alpha_i > 0$ and $\beta_i \in \mathbb{R}$. Since if $\mathbf{u}_i, i = 0, \dots, N$, are solutions to Eq. (35) then also $\mathbf{u}_i + C\mathbf{e}_i$ are solutions, we choose to set $\beta_0 = 0$ and remove this degree of freedom. Note as well that

$$\langle B_0 \boldsymbol{\lambda}, \mathbf{e}_0 \rangle = - \sum_{i=1}^N \langle B_i \boldsymbol{\lambda}, \mathbf{e}_i \rangle \quad \forall \boldsymbol{\lambda} \in \mathbb{R}^M, \quad (51)$$

hence Eq. (49) is replaced by the sufficient one

$$\langle B_i \boldsymbol{\lambda}, \mathbf{e}_i \rangle = 0, \quad i = 1, \dots, N. \quad (52)$$

Inserting Eq. (50) into Eq. (46) yields

$$\mathbf{V} = \sum_{i=0}^N B_i^\top (-\sigma_i^{-1} (P_i^+)^{-1} B_i \boldsymbol{\lambda} + \beta_i \mathbf{e}_i) = - \sum_{i=0}^N \sigma_i^{-1} B_i^\top (P_i^+)^{-1} B_i \boldsymbol{\lambda} + \sum_{i=1}^N \beta_i B_i^\top \mathbf{e}_i, \quad (53)$$

recall that $\beta_0 = 0$. From Eqs. (52) and (53) follow Eq. (41). \square

Now we use the result of Theorem 3.1 and the second equality of Eq. (39) in order to derive a standard ODE problem. We recall that $\mathbf{V}_0 = A_0 \mathbf{V}$.

Theorem 3.2. *The space discretization Eqs. (35) to (37) of Eq. (33) is equivalent to the ordinary differential equations system*

$$\begin{cases} C_m \mathbf{V}_0' + I_{ion}(\mathbf{V}_0, \mathbf{z}) = \psi(\mathbf{V}_0), \\ \mathbf{z}' = g(\mathbf{V}_0, \mathbf{z}), \end{cases} \quad (54a)$$

$$(54b)$$

where $\psi(\mathbf{V}_0) = \boldsymbol{\lambda}_0$ and $\boldsymbol{\lambda}_0 \in \mathbb{R}^{M_0}, \boldsymbol{\lambda}_g \in \mathbb{R}^{M_g}, \boldsymbol{\beta} \in \mathbb{R}^N$ are solutions to

$$\begin{pmatrix} F_{00} & F_{0g} & A_0 G \\ F_{g0} & F_{gg} - \kappa^{-1} I & A_g G \\ G^\top A_0^\top & G^\top A_g^\top & 0 \end{pmatrix} \begin{pmatrix} \boldsymbol{\lambda}_0 \\ \boldsymbol{\lambda}_g \\ \boldsymbol{\beta} \end{pmatrix} = \begin{pmatrix} \mathbf{V}_0 \\ \mathbf{0} \\ \mathbf{0} \end{pmatrix}, \quad (55)$$

with

$$F_{00} = A_0 F A_0^\top, \quad F_{0g} = A_0 F A_g^\top, \quad F_{g0} = A_g F A_0^\top, \quad F_{gg} = A_g F A_g^\top. \quad (56)$$

Proof. We denote $\mathbf{V}_g = A_g \mathbf{V}$, $\mathbf{V}_0 = A_0 \mathbf{V}$, $\boldsymbol{\lambda}_g = A_g \boldsymbol{\lambda}$ and $\boldsymbol{\lambda}_0 = A_0 \boldsymbol{\lambda}$. Also, note that $B_i^\top B_i = A_i^\top A_i$ since $B_i^\top B_i$ projects a global vector forth and back from Γ_i and if a sign change happens it occurs twice. Therefore

$$\left(\sum_{i=0}^N B_i^\top B_i \right) \mathbf{v} = \left(\sum_{i=0}^N A_i^\top A_i \right) \mathbf{v} = 2\mathbf{v} \quad \forall \mathbf{v} \in \mathbb{R}^M, \quad (57)$$

indeed every segment Γ_{ij} will receive the contribution from exactly two neighbouring domains. From Theorem 3.1 we have that $\psi_i(\mathbf{V}) = -B_i \boldsymbol{\lambda}$, which inserted into the second equality of Eq. (39) yields

$$\kappa \mathbf{V}_g = \kappa A_g \mathbf{V} = -\frac{1}{2} \sum_{i=1}^N A_g B_i^\top \psi_i(\mathbf{V}) = \frac{1}{2} A_g \left(\sum_{i=0}^N B_i^\top B_i \right) \boldsymbol{\lambda} = A_g \boldsymbol{\lambda} = \boldsymbol{\lambda}_g. \quad (58)$$

Note as well that $A_0^\top A_0 + A_g^\top A_g$ is the identity matrix in \mathbb{R}^M , hence multiplying the first line $F\boldsymbol{\lambda} + G\boldsymbol{\beta} = \mathbf{V}$ of Eq. (41) with A_0 yields

$$\mathbf{V}_0 = A_0 \mathbf{V} = A_0 F (A_0^\top A_0 \boldsymbol{\lambda} + A_g^\top A_g \boldsymbol{\lambda}) + A_0 G \boldsymbol{\beta} = F_{00} \boldsymbol{\lambda}_0 + F_{0g} \boldsymbol{\lambda}_g + A_0 G \boldsymbol{\beta}. \quad (59)$$

Similarly, multiplication by A_g yields $\mathbf{V}_g = F_{g0} \boldsymbol{\lambda}_0 + F_{gg} \boldsymbol{\lambda}_g + A_g G \boldsymbol{\beta}$ and thus

$$\mathbf{0} = F_{g0} \boldsymbol{\lambda}_0 + (F_{gg} - \kappa^{-1} I) \boldsymbol{\lambda}_g + A_g G \boldsymbol{\beta}. \quad (60)$$

For the second line of Eq. (41) we have

$$\mathbf{0} = G^\top \boldsymbol{\lambda} = G^\top A_0^\top \boldsymbol{\lambda}_0 + G^\top A_g^\top \boldsymbol{\lambda}_g. \quad (61)$$

Relations Eqs. (59) to (61) yield Eq. (55). The identity $-B_0 = A_0$ and $\psi_0(\mathbf{V}) = -B_0 \boldsymbol{\lambda} = A_0 \boldsymbol{\lambda} = \boldsymbol{\lambda}_0$ implies $\psi_0(\mathbf{V}) = \psi(\mathbf{V}_0)$ and hence Eq. (54). \square

From the proof of Theorem 3.2 we see that $\mathbf{V}, \boldsymbol{\lambda}$ of Theorem 3.1 are given by $\mathbf{V} = A_0^\top \mathbf{V}_0 + A_g^\top \mathbf{V}_g$, $\boldsymbol{\lambda} = A_0^\top \boldsymbol{\lambda}_0 + A_g^\top \boldsymbol{\lambda}_g$, $\kappa \mathbf{V}_g = \boldsymbol{\lambda}_g$ and moreover $\boldsymbol{\beta}$ is the same as in Theorem 3.1; hence, if needed, \mathbf{u}_i for $i = 0, \dots, N$ can be computed as in Theorem 3.1. Note as well that in Eq. (55) we have chosen to use $\boldsymbol{\lambda}_g$ as unknown, instead of the alternative \mathbf{V}_g . If we used \mathbf{V}_g we would obtain the same matrix as in Eq. (55) but with the second column multiplied by κ and therefore break the symmetry.

3.3 Time integration

For the time integration of Eq. (54), we use the multirate explicit stabilized method mRKC [1] for problems

$$\mathbf{y}' = f_F(t, \mathbf{y}) + f_S(t, \mathbf{y}), \quad \mathbf{y}(0) = \mathbf{y}_0, \quad (62)$$

where f_F is a stiff term and f_S is a mildly stiff but more expensive term. The mRKC scheme is fully explicit and does not have any step size restriction. Its stability properties are inherited from the RKC methods [13], which use an increased number of stages, with respect to classical methods, to increase stability. Since stability grows quadratically with the work load, the methods are particularly efficient. For the integration of Eq. (54) with mRKC, we rewrite Eq. (54) as Eq. (62), with

$$\mathbf{y} = \begin{pmatrix} \mathbf{V}_0 \\ \mathbf{z} \end{pmatrix}, \quad f_F(t, \mathbf{y}) = \begin{pmatrix} \psi(\mathbf{V}_0)/C_m \\ \mathbf{0} \end{pmatrix}, \quad f_S(t, \mathbf{y}) = \begin{pmatrix} -(I_{\text{ion}}(\mathbf{V}_0, \mathbf{z}) + I_{\text{stim}}(t))/C_m \\ g(\mathbf{V}_0, \mathbf{z}) \end{pmatrix}, \quad (63)$$

where $I_{\text{stim}}(t)$ is used to stimulate some cells and initiate an action potential propagation.

4 Numerical experiments

In this section we perform some numerical experiments in order to assess the accuracy of the space-time discretization of the cell-by-cell model (33) but also investigate the regularity properties of the model itself.

We start with two experiments, in Sections 4.1 and 4.2, where we investigate the convergence rates of the maps ψ_i from Theorem 3.1 and then the impact of the mesh and step size on the accuracy of the conduction velocity (CV). These experiments are crucial to understand which discretization parameters yield solutions within a certain error tolerance.

In the subsequent experiments the goal is to study the model itself. For instance, in Section 4.3 we investigate the effect of the gap junction's permeability κ on the CV and in Section 4.4 we study how the contact area between cells affects CV. Before presenting the results, we resume here below our computational setting.

Computational setup The following numerical experiments have been performed with our C++ code, where for the dense linear algebra routines we employ the **Eigen** library [17]. The ionic model, is taken from **CellML** [11] and the relative C code is produced with the **Myokit** library [9]. Concerning the model Eq. (33), the number of cells N and the domains Ω_i vary from one experiment to another and are specified later. If not stated otherwise, in the next experiments we use the coefficients C_m , σ_i , κ , given in Table 1. The values for C_m , σ_i , κ are taken from [40], where for κ we consider $\kappa = 1/R_m$ with $R_m = 0.00145 \text{ k}\Omega \text{ cm}^2$. If not specified, we consider the ionic model from (author?) [10]. The initial values for V for and the ionic model's state variables are uniform on the transmembrane boundary and are taken from the Myokit's code. For instance, for the Courtemanche-Nattel-Ramírez model the initial value for V is $V_0 = -81.18 \text{ mV}$.

C_m	σ_0	$\sigma_1, \dots, \sigma_N$	κ
$1 \mu\text{F cm}^{-2}$	20 mS cm^{-1}	3 mS cm^{-1}	690 mS cm^{-2}

Table 1: Model's coefficients employed in numerical experiments.

4.1 Approximation properties of the ψ operators

In this experiment we investigate the convergence rate of the ψ_i operators defined in Theorem 3.1. For this purpose, we conduct four convergence experiments, one for every geometry displayed in Fig. 3, and we display the errors on the trace and normal derivative against the number of degrees of freedom M in Fig. 4.

Let us describe the geometries of Fig. 3. In Fig. 3a we have a model composed of one cell ($N = 1$), defined by $\Omega_0 = \{\mathbf{x} \in \mathbb{R}^2 : 2 < \|\mathbf{x}\| < 4\}$ and $\Omega_1 = \{\mathbf{x} \in \mathbb{R}^2 : \|\mathbf{x}\| < 2\}$. In Fig. 3b we split the cell by introducing a vertical gap junction, hence we have the same Ω_0 but $\Omega_1 = \{\mathbf{x} \in \mathbb{R}^2 : \|\mathbf{x}\| < 2, x_1 < 0\}$ and $\Omega_2 = \{\mathbf{x} \in \mathbb{R}^2 : \|\mathbf{x}\| < 2, x_1 > 0\}$. In Fig. 3c we keep the same cells but remove the gap junction by

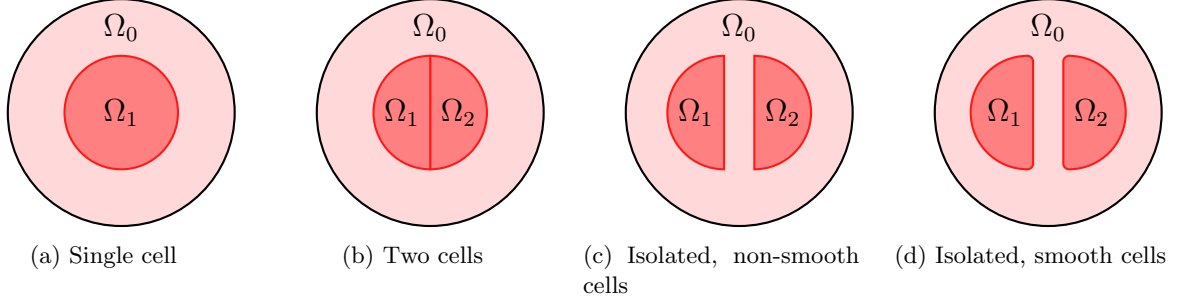


Figure 3: Illustration of the geometrical settings employed in Section 4.1.

introducing an horizontal gap of size 0.4 between Ω_1 and Ω_2 . Finally, in Fig. 3d we keep the separation of Ω_1 , Ω_2 but smooth out the corners by introducing quarter of circles of radius 0.2 μm .

For the setting of Figs. 3a and 3b an exact solution to Eqs. (34a) to (34d), with V defined by Eq. (34c), is given by

$$u_0(\mathbf{x}) = \frac{\sigma_1}{\sigma_0} \frac{16 + \|\mathbf{x}\|^2}{6\|\mathbf{x}\|^2} x_2, \quad u_1(\mathbf{x}) = u_2(\mathbf{x}) = -\frac{1}{2}x_2. \quad (64)$$

Therefore, for different values of M (i.e. number of collocation points), we can compute the vector of coefficients \mathbf{u}_i , define \mathbf{V} as in Eq. (35), solve Eq. (41) and compute the errors

$$e_1 = \max_{i=0,\dots,N} \|\psi_i(\mathbf{V}) - \sigma_i \partial_{\mathbf{n}_i} u_i\|_{L^2(\Gamma_i)}, \quad e_0 = \max_{i=0,\dots,N} \|\tilde{\psi}_i(\mathbf{V}) - u_i\|_{L^2(\Gamma_i)/\mathbb{R}}, \quad (65)$$

where $\tilde{\psi}_i(\mathbf{V}) = -\sigma_i^{-1}(P_i^+)^{-1} B_i \boldsymbol{\lambda} + \beta_i \mathbf{e}_i$ and thus $\tilde{\psi}_i(\mathbf{V}_m)$ approximates u_i (cf. Eq. (44)), up to a constant.

For the geometries of Figs. 3c and 3d we do not possess an exact solution. Hence, we set $V(\mathbf{x}) = \cos(\pi x_1) \sin(\pi x_2)$ and errors e_1 , e_0 are now computed as

$$e_1 = \max_{i=0,\dots,N} \|\psi_i(\mathbf{V}) - \psi_i(\mathbf{V}^*)\|_{L^2(\Gamma_i)}, \quad e_0 = \max_{i=0,\dots,N} \|\tilde{\psi}_i(\mathbf{V}) - \tilde{\psi}_i(\mathbf{V}^*)\|_{L^2(\Gamma_i)/\mathbb{R}}, \quad (66)$$

where $\psi_i(\mathbf{V}^*)$, $\tilde{\psi}_i(\mathbf{V}^*)$ are reference solutions calculated on a finer mesh.

We display the errors e_0, e_1 with respect to M , for the geometries of Fig. 3, in Fig. 4. Due to the smoothness of the solutions and the boundaries, we remark in Fig. 4a that for the first problem we obtain exponential convergence thanks to the trigonometric Lagrange basis functions; with very few degrees of freedom machine precision is achieved. This result is in line with the theory and experiments performed in [19]. In the second problem, the boundary is Lipschitz continuous only, which prevents exponential convergence. Indeed, in Fig. 4b the convergence rates for the trace and normal derivative are 1.5 and 0.5, respectively.

In Figs. 4a and 4b we see how the convergence rates decrease dramatically when the circle is divided into two half-circles. The purpose of two last experiments is to demonstrate numerically that this phenomenon is due to the non smooth boundaries, rather than the introduction of a gap junction. Indeed, in Fig. 4c we observe the same convergence rates as in Fig. 4b, while in Fig. 4d we obtain higher convergence rates.

4.2 Impact of discretization parameters on conduction velocity

It is already known that discretization methods, mesh size and step size affect conduction velocity (CV) in the monodomain and bidomain models for cardiac electrophysiology [8, 32, 33]. In this experiment we investigate how mesh and step size affect the CV for the cell-by-cell model discretized with the BEM in space and the mRKC method [1] in time. In order to be able to employ relatively uniform mesh sizes in this experiment we consider rectangular cells.

To measure the CV we design the following experiment. We consider an array of 2×30 connected rectangular cells of width $c_w = 20 \mu\text{m}$ and length $c_l = 100 \mu\text{m}$, cells are positioned so that their bottom left vertex has coordinates $(i \cdot c_l, j \cdot c_w)$ for $i = 0, \dots, 29$, $j = 0, 1$; yielding a block of cells of width $2 \cdot c_w = 40 \mu\text{m}$ and length $30 \cdot c_l = 3000 \mu\text{m}$. The outer domain is a rectangle of size $440 \mu\text{m} \times 5000 \mu\text{m}$ centred on the array of cells. To initiate an action potential traversing the cell's array a stimulus of $300 \mu\text{A cm}^{-2}$ is applied for a duration of 1 ms at the transmembrane boundary of the two leftmost

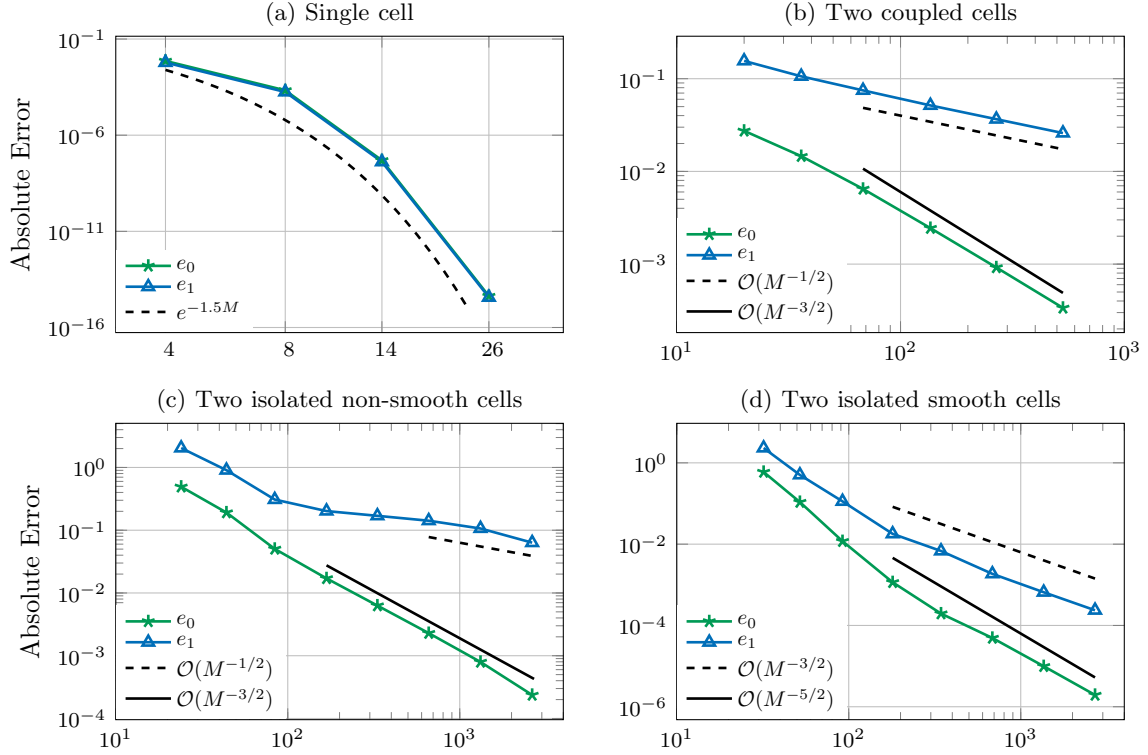


Figure 4: Convergence rates of the ψ operator defined in Theorem 3.1 for the problems depicted in Fig. 3.



Figure 5: Action potential propagation in an array of 2×20 cells ($t = 2$ ms).

cells. CV is computed as the average over $CV_k = \|\mathbf{p}_k - \mathbf{q}_k\| / (t_{\mathbf{p}_k} - t_{\mathbf{q}_k})$ for $k = 1, \dots, 5$, where: $\mathbf{p}_k = ((7.5 + k) \cdot c_l) \mu\text{m}$, $\mathbf{q}_k = ((17.5 + k) \cdot c_l, 0) \mu\text{m}$ and $t_{\mathbf{p}_k}, t_{\mathbf{q}_k}$ are the time instants in which V exceeds the threshold of $V_{\text{th}} = -20$ mV in $\mathbf{p}_k, \mathbf{q}_k$, respectively. The choice of $\mathbf{p}_k, \mathbf{q}_k$ is such that measures are taken sufficiently far from the stimulated point and to avoid boundary effects as well. See Fig. 5 for an illustration of the solution at time $t = 2$ ms.

We solve Eq. (54) with different step sizes Δt and mesh size Δx and compute the signed relative error on CV: $E_{\text{CV}} = (CV - CV^*) / CV^*$, with CV^* a reference solution. We display E_{CV} as function of $\Delta t, \Delta x$ in Fig. 6. The reference value of CV is $CV^* \approx 1.27153$.

First, we notice that for coarse space grids the true CV^* tends to be overestimated, whereas for large time steps it is underestimated. Then, we remark that even with relatively large mesh sizes $\Delta x = 20 \mu\text{m}$ the estimated CV remains within a 2% error. Figure 6 (middle and right panels) also shows the same results, but for the unsigned relative error $|E_{\text{CV}}|$ and fixing either Δx or Δt . We observe that the local minimal appearing in the curves is due to the cancellation of the positive spatial discretization error with the negative time discretization error.

Based on the results of this section, in the forthcoming experiments we consider $\Delta t \leq 0.02$ ms and $\Delta x \leq 10 \mu\text{m}$, which, for this experiment, yield a relative error of less than 5%.

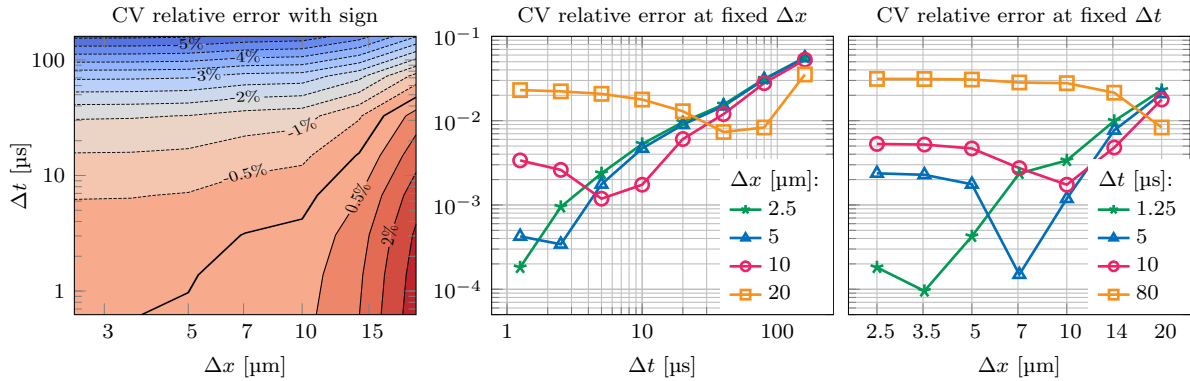


Figure 6: Conduction velocity accuracy with respect to timestep Δt and mesh size Δx .

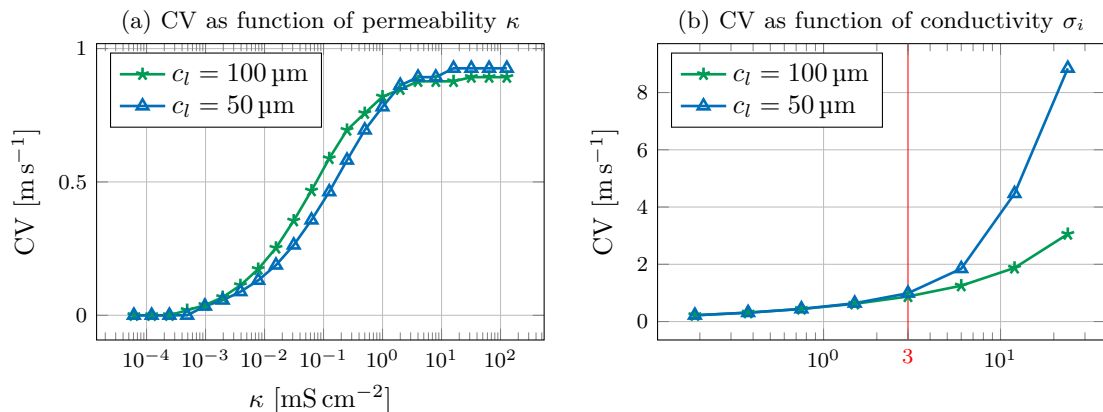


Figure 7: Dependence of CV on permeability κ and intracellular conductivity σ_i (red: reference value).

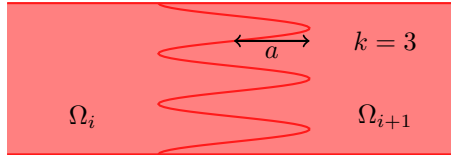
4.3 Dependence of conduction velocity on gap junctions' permeability and cells inner conductivity

In this experiment we study how CV depends on the gap junctions' permeability κ and the inner conductivity σ_i , $i = 1, \dots, N$. For that purpose, we consider again an array of 2×30 cells and cells of size $c_w \times c_l$, with fixed $c_w = 10 \mu\text{m}$ and either $c_l = 100 \mu\text{m}$ or $c_l = 50 \mu\text{m}$. First, we measure CV for varying κ but keeping the other coefficients fixed, a stimulus is initiated applying a stimulus of $200 \mu\text{A cm}^{-2}$ to the transmembrane boundary of the two leftmost cells. Results for $c_l = 100 \mu\text{m}$ and $c_l = 50 \mu\text{m}$ are displayed in Fig. 7a. We observe as CV decreases with κ and also that the physiological value $\kappa = 690$ is in the range where CV is maximal. We note that for values of $\kappa \leq 2 \cdot 10^{-4}$ the action potential does not propagate. Then, we measure CV for varying σ_i , $i = 1, \dots, N$, and fixed κ , results are displayed in Fig. 7b for $c_l = 100 \mu\text{m}$ and $c_l = 50 \mu\text{m}$. Conduction velocity increases with σ_i , specially for the shorter cells.

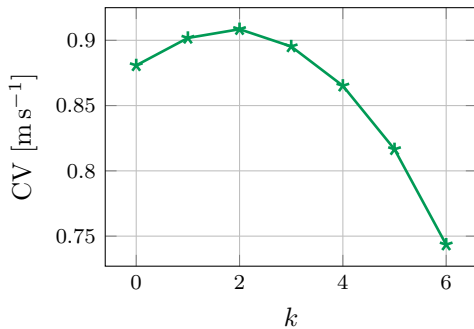
4.4 Dependence of conduction velocity on gap junctions' surface area

In general, gap junctions perpendicular to the fiber direction are not flat surfaces and are better modelled by intercalated discs [21]. In two dimensions we model these gap junctions with a sinus wave (see Fig. 8a for an illustration) of amplitude a and frequency k .

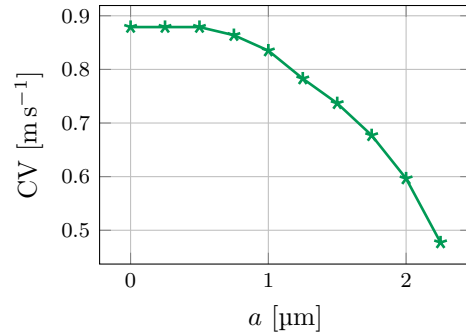
In this experiment we consider an array of 2×30 cells of size $10 \mu\text{m} \times 100 \mu\text{m}$ and measure CV as in Section 4.2. In Fig. 8b we show the conduction velocity as a function of the frequency k for a fixed amplitude of $a = 0.5 \mu\text{m}$. We note that for moderate frequency k the CV increases due to an increase of contact surface area. However, for larger frequencies CV decreases, probably because of a flux saturation at the narrower junctions. In Fig. 8c we show the conduction velocity as a function of the amplitude a for a fixed frequency of $k = 3$. Again, for larger amplitude a the conduction velocity decreases.



(a) Two cells with an intercalated discs at gap junctions.



(b) Impact of intercalated discs frequency on CV for $a = 0.5 \mu\text{m}$.



(c) Impact of intercalated discs amplitude on CV for $k = 3$.

Figure 8: Effect of gap junctions surface area on CV.

4.5 Dependence of conduction velocity on cells size and aspect ratio

Finally, we investigate how the cell's size and aspect ratio impact the conduction velocity. We consider an array of 2×30 cells of size $c_w \times c_l$. First, we fix $c_w = 10 \mu\text{m}$ and vary c_l , results are reported in Fig. 9b. We observe as CV decreases as c_l increases. In Fig. 9a we display the results for fixed $c_l = 100 \mu\text{m}$ and varying c_w , here CV increases with c_w . In the last figure Fig. 9c we vary both c_l and c_w while keeping a constant aspect ratio $c_l = 10 \cdot c_w$, more precisely they vary from $(c_w, c_l) = (2.5 \mu\text{m}, 25 \mu\text{m})$ to $(c_w, c_l) = (14 \mu\text{m}, 140 \mu\text{m})$. We see as CV increases with the cells area $A = c_l \cdot c_w$.

5 Conclusion

In this paper we solve the cell-by-cell or EMI model for cardiac electrophysiology via the boundary element method, with no geometrical restrictions. The cell-by-cell model consists in Laplace equations inside and outside the cellular domains coupled with an ordinary differential equation on the transmembrane boundary and an algebraic condition on the gap junctions. Due to the boundary integral formulation, Laplace equations are cleared away, yielding a differential algebraic equation living on the cell's boundaries only. In a subsequent step, the differential algebraic equation is reduced to an ordinary differential equation lying on the transmembrane boundary only. Finally, we provide numerical results where: first, we study the accuracy of the numerical method and then we investigate the model properties and sensibility with respect to its parameters.

The convergence rate shows that the solution of the general problem is non-smooth, due to the presence of multiple cell contact (or 2 cells and the extracellular domain.) The single cell problem is instead smooth. To the best of our knowledge, there are no regularity results for the single cell problem, except for those provided in [29] on asymptotic solutions. For the one-cell problem (1) with smooth interface, but $\sigma_1 \neq \sigma_0$, the solution is probably regular. Intuitively, the interface problem with piecewise smooth coefficients and fixed transmembrane potential (that is, at the equilibrium) can be recast, via lifting [7], to a more classical interface problem already studied by (author?) [2, 23], who showed that the solution is at least H^2 on each subdomain.

Well-posedness results for the general EMI problem are found in [3, 15], however we are not aware of regularity results for the general EMI problem (33). For two or more cells in contact, subdomains must be polygonal, which limits the regularity. The singularities introduced by the contact have been analyzed by (author?) [31]. Moreover, the transmembrane voltage cannot be smooth on Γ_0 , because

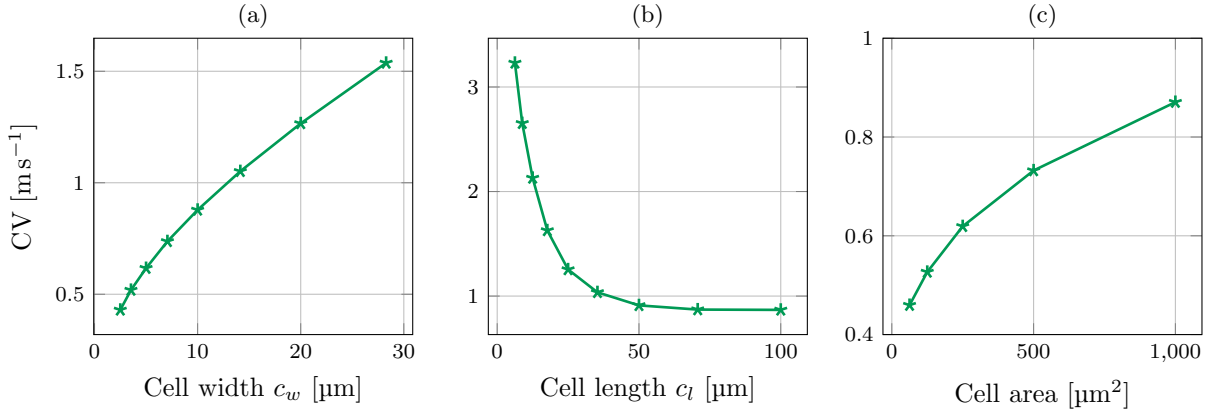


Figure 9: Impact of cell length c_l , cell width c_w , and cell area with fixed aspect ratio on the CV.

it has multiple branches. These results should be taken in consideration in the development of higher order numerical schemes for the solution of the EMI problem.

We also show that the discretization parameters are not too restrictive, when compared to the more standard (homogenized) bidomain model. A typical time step is 0.02 ms or lower for IMEX solvers [25]. In space, we observed here that a mesh resolution for the membrane of 10 μm is sufficiently accurate for the cell-by-cell model. On the other hand, for the standard bidomain the mesh size depends on the front thickness, in turn depending on tissue excitability and conductivity. An accepted value is 100 μm to 200 μm [32]. However, this is only true in the fiber direction and for healthy tissue, since in fibrotic tissue or in the cross-fiber direction the front thickness is generally lower [33, 34]. Finally, we observed here that propagation failure can occur in the EMI model, in contrast to the bidomain model. This aspect is very important in the study of pathological situations.

This work paves the way in two directions. First, for designing another method where a more realistic cell-by-cell model is solved, i.e., where the linear algebraic condition on the gap junctions is replaced by a stiff nonlinear ordinary differential equation. Second, it provides the mathematical framework for solving the EMI model in three dimensions with a boundary integral formulation. Once assembled, the solution of the problem is very fast, opening interesting opportunities for long simulations.

Acknowledgement

We are very grateful to Michael Multerer for kindly sharing the BEM code and the fruitful discussion on the problem. We also thank the MICROCARD consortium for the suggestions for improving the manuscript.

References

- [1] Assyr Abdulle, Marcus J. Grote, and Giacomo Rosilho de Souza. Explicit stabilized multirate method for stiff differential equations. *Mathematics of Computation*, 91:2681–2714, 2022.
- [2] Ivo Babuška. The finite element method for elliptic equations with discontinuous coefficients. *Computing*, 5(3):207–213, 1970.
- [3] Pierre-Elliott Bécue. *Modélisation et simulation de l'électrophysiologie cardiaque à l'échelle microscopique*. Theses, Université de Bordeaux, December 2018.
- [4] Pierre-Elliott Bécue, Florian Caro, Mark Potse, and Yves Coudière. Theoretical and Numerical Study of Cardiac Electrophysiology Problems at the Microscopic Scale. SIAM Conference on the Life Sciences (LS16), July 2016. Poster.
- [5] Pierre-Elliott Bécue, Mark Potse, and Yves Coudière. Microscopic simulation of the cardiac electrophysiology: A study of the influence of different gap junctions models. In *2018 Computing in Cardiology Conference (CinC)*, volume 45, pages 1–4. IEEE, 2018.

- [6] Pierre-Elliott Bécue, Mark Potse, and Yves Coudière. A three-dimensional computational model of action potential propagation through a network of individual cells. In *2017 Computing in Cardiology (CinC)*, pages 1–4, 2017.
- [7] Zhiming Chen and Jun Zou. Finite element methods and their convergence for elliptic and parabolic interface problems. *Numerische Mathematik*, 79(2):175–202, 1998.
- [8] R. H. Clayton, O. Bernus, E. M. Cherry, H. Dierckx, F. H. Fenton, L. Mirabella, A. V. Panfilov, F. B. Sachse, G. Seemann, and H. Zhang. Models of cardiac tissue electrophysiology: Progress, challenges and open questions. *Progress in Biophysics and Molecular Biology*, 104:22–48, 2011.
- [9] Michael Clerx, Pieter Collins, Enno de Lange, and Paul G.A. Volders. Myokit: A simple interface to cardiac cellular electrophysiology. *Progress in Biophysics and Molecular Biology*, 120:100–114, 1 2016.
- [10] Marc Courtemanche, Rafael J Ramirez, and Stanley Nattel. Ionic mechanisms underlying human atrial action potential properties: insights from a mathematical model. *American Journal of Physiology-Heart and Circulatory Physiology*, 275:H301–H321, 1998.
- [11] Autumn A. Cuellar, Catherine M. Lloyd, Poul F. Nielsen, David P. Bullivant, David P. Nickerson, and Peter J. Hunter. An overview of cellml 1.1, a biological model description language. *SIMULATION*, 79:740–747, 12 2003.
- [12] Cécile Daversin-Catty, Chris N Richardson, Ada J Ellingsrud, and Marie E Rognes. Abstractions and automated algorithms for mixed domain finite element methods. *ACM Transactions on Mathematical Software (TOMS)*, 47(4):1–36, 2021.
- [13] P. J. Van der Houwen and B. P. Sommeijer. On the internal stability of explicit, m -stage runge–kutta methods for large m -values. *Zeitschrift für Angewandte Mathematik und Mechanik*, 60:479–485, 1980.
- [14] K. R. Foster and A. E. Sowers. Dielectrophoretic forces and potentials induced on pairs of cells in an electric field. *Biophysical Journal*, 69:777–784, 1995.
- [15] Piero Colli Franzone and Giuseppe Savaré. Degenerate evolution systems modeling the cardiac electric field at micro-and macroscopic level. *Evolution Equations, Semigroups and Functional Analysis: in memory of Brunello Terreni*, pages 49–78, 2002.
- [16] Lia Gander, Rolf Krause, Michael Multerer, and Simone Pezzuto. Space–time shape uncertainties in the forward and inverse problem of electrocardiography. *International Journal for Numerical Methods in Biomedical Engineering*, 37:1–23, 2021.
- [17] Gaël Guennebaud, Benoît Jacob, et al. Eigen v3. <http://eigen.tuxfamily.org>, 2010.
- [18] Paul E Hand, Boyce E Griffith, and Charles S Peskin. Deriving macroscopic myocardial conductivities by homogenization of microscopic models. *Bulletin of Mathematical Biology*, 71:1707–1726, 2009.
- [19] Fernando Henríquez and Carlos Jerez-Hanckes. Multiple traces formulation and semi-implicit scheme for modelling biological cells under electrical stimulation. *ESAIM: Mathematical Modelling and Numerical Analysis*, 52:659–702, 2018.
- [20] Fernando Henríquez, Carlos Jerez-Hanckes, and Fernando Altermatt. Boundary integral formulation and semi-implicit scheme coupling for modeling cells under electrical stimulation. *Numerische Mathematik*, 136:101–145, 5 2017.
- [21] Hervé Hogues, L. Joshua Leon, and Fernand A. Roberge. A model study of electric field interactions between cardiac myocytes. *IEEE Transactions on Biomedical Engineering*, 39:1232–1243, 1992.
- [22] Karoline Horgmo Jæger, Andrew G. Edwards, Wayne R. Giles, and Aslak Tveito. Arrhythmogenic influence of mutations in a myocyte-based computational model of the pulmonary vein sleeve. *Scientific Reports*, 12, 12 2022.
- [23] Bruce R Kellogg. On the poisson equation with intersecting interfaces. *Applicable Analysis*, 4(2):101–129, 1974.

- [24] André G Kléber and Yoram Rudy. Basic mechanisms of cardiac impulse propagation and associated arrhythmias. *Physiological reviews*, 2004.
- [25] Dorian Krause, Mark Potse, Thomas Dickopf, Rolf Krause, Angelo Auricchio, and Frits W. Prinzen. Hybrid parallelization of a large-scale heart model. In Rainer Keller, David Kramer, and Jan-Philipp Weiss, editors, *Facing the Multicore-Challenge II*, volume 7174 of *Lecture Notes in Computer Science*, pages 120–132, Berlin, 2012. Springer.
- [26] Rainer Kress. *Linear Integral Equations*. Springer, 1989.
- [27] U. Langer and O. Steinbach. Boundary element tearing and interconnecting methods. *Computing*, 71:205–228, 2003.
- [28] L. J. Leon and F. A. Roberge. A model study of extracellular stimulation of cardiac cells. *IEEE Transactions on Biomedical Engineering*, 40:1307–1319, 1993.
- [29] Hiroshi Matano and Yoichiro Mori. Global existence and uniqueness of a three-dimensional model of cellular electrophysiology. *Discrete Contin. Dyn. Syst.*, 29(4):1573–1636, 2011.
- [30] JC Neu and W Krassowska. Homogenization of syncytial tissues. *Critical reviews in biomedical engineering*, 21(2):137–199, 1993.
- [31] Serge Nicaise and Anna-Margarete Sändig. General interface problems—i. *Mathematical Methods in the Applied Sciences*, 17(6):395–429, 1994.
- [32] Steven A. Niederer, Eric Kerfoot, Alan P. Benson, Miguel O. Bernabeu, Olivier Bernus, Chris Bradley, Elizabeth M. Cherry, Richard Clayton, Flavio H. Fenton, Alan Garny, Elvio Heidenreich, Sander Land, Mary Maleckar, Pras Pathmanathan, Gernot Plank, José F. Rodríguez, Ishani Roy, Frank B. Sachse, Gunnar Seemann, Ola Skavhaug, and Nic P. Smith. Verification of cardiac tissue electrophysiology simulators using an n-version benchmark. *Philosophical Transactions of the Royal Society A: Mathematical, Physical and Engineering Sciences*, 369:4331–4351, 2011.
- [33] Simone Pezzuto, J. Hake, and Joakim Sundnes. Space-discretization error analysis and stabilization schemes for conduction velocity in cardiac electrophysiology. *International Journal for Numerical Methods in Biomedical Engineering*, 32:e02762, 2016. Referenze 12,13,14.
- [34] Carlos Ruiz Herrera, Thomas Grandits, Gernot Plank, Paris Perdikaris, Francisco Sahli Costabal, and Simone Pezzuto. Physics-informed neural networks to learn cardiac fiber orientation from multiple electroanatomical maps. *Engineering with Computers*, 38(5):3957–3973, 2022.
- [35] Stefan A. Sauter and Cristoph Schwab. *Boundary element methods*. Springer, 2011.
- [36] Ulrich Schotten, Sander Verheule, Paulus Kirchhof, and Andreas Goette. Pathophysiological mechanisms of atrial fibrillation: a translational appraisal. *Physiological Reviews*, 91(1):265–325, 2011.
- [37] Madison S Spach and J Francis Heidlage. The stochastic nature of cardiac propagation at a microscopic level: electrical description of myocardial architecture and its application to conduction. *Circulation research*, 76(3):366–380, 1995.
- [38] Olaf Steinbach. *Numerical Approximation Methods for Elliptic Boundary Value Problems: Finite and Boundary Elements*. Springer, 2007.
- [39] Jeroen Stinstra, Rob MacLeod, and Craig Henriquez. Incorporating histology into a 3d microscopic computer model of myocardium to study propagation at a cellular level. *Annals of Biomedical Engineering*, 38:1399–1414, 4 2010.
- [40] Jeroen G. Stinstra, Bruce Hopenfeld, and Rob S. MacLeod. On the passive cardiac conductivity. *Annals of Biomedical Engineering*, 33:1743–1751, 2005.
- [41] JG Stinstra, CS Henriquez, and RS MacLeod. Comparison of microscopic and bidomain models of anisotropic conduction. *Computers in Cardiology*, 36:657–660, 2009.
- [42] JG Stinstra, S Poelzing, RS MacLeod, and CS Henriquez. A model for estimating the anisotropy of the conduction velocity in cardiac tissue based on the tissue morphology. *Computers in Cardiology*, 34:129–132, 2007.

- [43] Aslak Tveito, Karoline H. Jæger, Miroslav Kuchta, Kent Andre Mardal, and Marie E. Rognes. A cell-based framework for numerical modeling of electrical conduction in cardiac tissue. *Frontiers in Physics*, 5, 10 2017.
- [44] Aslak Tveito, Kent-Andre Mardal, and Marie E Rognes. *Modeling Excitable Tissue: The EMI Framework*. Springer Nature, 2021.
- [45] Edward J Vigmond, Jose L Perez Velazquez, Taufik A Valiante, Berj L Bardakjian, and Peter L Carlen. Mechanisms of electrical coupling between pyramidal cells. *Journal of Neurophysiology*, 78(6):3107–3116, 1997.

A Poincaré–Steklov map on Ω_0

Here we briefly describe how to derive the Poincaré–Steklov operators \mathcal{P}_0, P_0 on Ω_0 used in Eqs. (9) and (17), respectively.

Let $\Phi \in \{\Gamma_0, \Sigma\}$, we introduce the restricted trace operators

$$\begin{aligned} \gamma_{t,\Phi}^0: H^1(\Omega_0) &\rightarrow H^{1/2}(\Phi), & \gamma_{t,\Phi}^0 u_0(\mathbf{x}) &= \lim_{\Omega_0 \ni \mathbf{y} \rightarrow \mathbf{x} \in \Phi} u_0(\mathbf{y}), \\ \gamma_{n,\Phi}^0: H^1(\Omega_0) &\rightarrow H^{-1/2}(\Phi), & \gamma_{n,\Phi}^0 u_0(\mathbf{x}) &= \lim_{\Omega_0 \ni \mathbf{y} \rightarrow \mathbf{x} \in \Phi} \langle \nabla u_0(\mathbf{y}), \mathbf{n}_0 \rangle. \end{aligned} \quad (67)$$

From the Green’s representation formula we have

$$\begin{aligned} u_0(\mathbf{x}) &= \int_{\Gamma_0} \gamma_{t,\mathbf{y}}^0 G(\mathbf{x}, \mathbf{y}) \gamma_{n,\Gamma_0}^0 u_0(\mathbf{y}) \, ds_{\mathbf{y}} + \int_{\Sigma} \gamma_{t,\mathbf{y}}^0 G(\mathbf{x}, \mathbf{y}) \gamma_{n,\Sigma}^0 u_0(\mathbf{y}) \, ds_{\mathbf{y}} \\ &\quad - \int_{\Gamma_0} \gamma_{n,\mathbf{y}}^0 G(\mathbf{x}, \mathbf{y}) \gamma_{t,\Gamma_0}^0 u_0(\mathbf{y}) \, ds_{\mathbf{y}} - \int_{\Sigma} \gamma_{n,\mathbf{y}}^0 G(\mathbf{x}, \mathbf{y}) \gamma_{t,\Sigma}^0 u_0(\mathbf{y}) \, ds_{\mathbf{y}}, \quad \mathbf{x} \in \Omega_0. \end{aligned} \quad (68)$$

For $\Phi, \Psi \in \{\Gamma_0, \Sigma\}$, we define

$$\begin{aligned} \mathcal{V}_0^{\Psi,\Phi}: H^{-1/2}(\Phi) &\rightarrow H^{1/2}(\Psi), & \mathcal{V}_0^{\Psi,\Phi} \rho(\mathbf{x}) &= \int_{\Phi} \gamma_{0,\mathbf{y}}^0 G(\mathbf{x}, \mathbf{y}) \rho(\mathbf{y}) \, ds_{\mathbf{y}}, & \mathbf{x} \in \Psi, \\ \mathcal{K}_0^{\Psi,\Phi}: H^{1/2}(\Phi) &\rightarrow H^{1/2}(\Psi), & \mathcal{K}_0^{\Psi,\Phi} \rho(\mathbf{x}) &= \int_{\Phi} \gamma_{1,\mathbf{y}}^0 G(\mathbf{x}, \mathbf{y}) \rho(\mathbf{y}) \, ds_{\mathbf{y}}, & \mathbf{x} \in \Psi, \end{aligned} \quad (69)$$

applying the trace operators γ_{t,Γ_0}^0 and $\gamma_{n,\Sigma}^0$ to Eq. (68) yields

$$\begin{aligned} \gamma_{t,\Gamma_0}^0 u_0 &= \mathcal{V}_0^{\Gamma_0,\Gamma_0} \gamma_{n,\Gamma_0}^0 u_0 + \mathcal{V}_0^{\Gamma_0,\Sigma} \gamma_{n,\Sigma}^0 u_0 - (\mathcal{K}_0^{\Gamma_0,\Gamma_0} - \frac{1}{2}I) \gamma_{t,\Gamma_0}^0 u_0 - \mathcal{K}_0^{\Gamma_0,\Sigma} \gamma_{t,\Sigma}^0 u_0, \\ \gamma_{t,\Sigma}^0 u_0 &= \mathcal{V}_0^{\Sigma,\Gamma_0} \gamma_{n,\Gamma_0}^0 u_0 + \mathcal{V}_0^{\Sigma,\Sigma} \gamma_{n,\Sigma}^0 u_0 - \mathcal{K}_0^{\Sigma,\Gamma_0} \gamma_{t,\Gamma_0}^0 u_0 - (\mathcal{K}_0^{\Sigma,\Sigma} - \frac{1}{2}I) \gamma_{t,\Sigma}^0 u_0, \end{aligned} \quad (70)$$

which, after manipulation and setting $\gamma_{n,\Sigma}^0 u_0 = 0$ (cf. Eq. (33g)), result in

$$\begin{aligned} (\mathcal{K}_0^{\Gamma_0,\Gamma_0} + \frac{1}{2}I) \gamma_{t,\Gamma_0}^0 u_0 &= \mathcal{V}_0^{\Gamma_0,\Gamma_0} \gamma_{n,\Gamma_0}^0 u_0 - \mathcal{K}_0^{\Gamma_0,\Sigma} \gamma_{t,\Sigma}^0 u_0, \\ (\mathcal{K}_0^{\Sigma,\Sigma} + \frac{1}{2}I) \gamma_{t,\Sigma}^0 u_0 &= \mathcal{V}_0^{\Sigma,\Gamma_0} \gamma_{n,\Gamma_0}^0 u_0 - \mathcal{K}_0^{\Sigma,\Gamma_0} \gamma_{t,\Gamma_0}^0 u_0. \end{aligned} \quad (71)$$

Solving for $\gamma_{n,\Gamma_0}^0 u_0, \gamma_{t,\Sigma}^0 u_0$ with respect to $\gamma_{t,\Gamma_0}^0 u_0$ yields the linear relation Eq. (9) (dropping Γ_0 from the notation).

We discretize $\Gamma_0 = \Gamma_1$ as in Section 2.2 (same collocation points) and place \overline{M} collocation points $\overline{\mathbf{x}}_j$ on Σ . We compute a smooth parametrization $\gamma_{\Sigma}: [0, 1] \rightarrow \mathbb{R}^d$ of Σ , $\gamma_{\Sigma}(s_j) = \overline{\mathbf{x}}_j$, by Fourier interpolation (as for Γ_0) and represent

$$\begin{aligned} \gamma_{t,\Gamma_0}^0 u_0(\gamma_{\Gamma_0}(t)) &= \sum_{j=1}^M u_{0,\Gamma_0}^j L_j(t), & \gamma_{n,\Gamma_0}^0 u_0(\gamma_{\Gamma_0}(t)) &= \sum_{j=1}^M \tilde{u}_{0,\Gamma_0}^j L_j(t), \\ \gamma_{t,\Sigma}^0 u_0(\gamma_{\Sigma}(t)) &= \sum_{j=1}^{\overline{M}} u_{0,\Sigma}^j \overline{L}_j(t), \end{aligned} \quad (72)$$

with $\bar{L}_j(s)$ the trigonometric Lagrange basis functions satisfying $\bar{L}_j(s_i) = \delta_{ij}$, $i, j = 1, \dots, \bar{M}$. Inserting Eq. (72) into Eq. (71) yields

$$\begin{aligned} (K_0^{\Gamma_0, \Gamma_0} + \frac{1}{2}I)\mathbf{u}_{0, \Gamma_0} &= V_0^{\Gamma_0, \Gamma_0} \tilde{\mathbf{u}}_{0, \Gamma_0} - K_0^{\Gamma_0, \Sigma} \mathbf{u}_{0, \Sigma}, \\ (K_0^{\Sigma, \Sigma} + \frac{1}{2}\bar{I})\mathbf{u}_{0, \Sigma} &= V_0^{\Sigma, \Gamma_0} \tilde{\mathbf{u}}_{0, \Gamma_0} - K_0^{\Sigma, \Gamma_0} \mathbf{u}_{0, \Gamma_0}, \end{aligned} \quad (73)$$

with $(\mathbf{u}_{0, \Gamma_0})_j = u_{0, \Gamma_0}^j$, $(\tilde{\mathbf{u}}_{0, \Gamma_0})_j = \tilde{u}_{0, \Gamma_0}^j$, $(\mathbf{u}_{0, \Sigma})_j = u_{0, \Sigma}^j$ and

$$(K_0^{\Gamma_0, \Gamma_0})_{kj} = \mathcal{K}_0^{\Gamma_0, \Gamma_0}(L_j \circ \gamma_{\Gamma_0}^{-1})(\mathbf{x}_k), \quad (K_0^{\Sigma, \Gamma_0})_{kj} = \mathcal{K}_0^{\Sigma, \Gamma_0}(L_j \circ \gamma_{\Gamma_0}^{-1})(\bar{\mathbf{x}}_k), \quad (74)$$

$$(K_0^{\Sigma, \Sigma})_{kj} = \mathcal{K}_0^{\Sigma, \Sigma}(\bar{L}_j \circ \gamma_{\Sigma}^{-1})(\bar{\mathbf{x}}_k), \quad (K_0^{\Gamma_0, \Sigma})_{kj} = \mathcal{K}_0^{\Gamma_0, \Sigma}(\bar{L}_j \circ \gamma_{\Sigma}^{-1})(\mathbf{x}_k), \quad (75)$$

and similarly for V_0^{Σ, Γ_0} , $V_0^{\Gamma_0, \Gamma_0}$. Solving for $\tilde{\mathbf{u}}_{0, \Gamma_0}$, $\mathbf{u}_{0, \Sigma}$ with respect to \mathbf{u}_{0, Γ_0} yields

$$\tilde{\mathbf{u}}_{0, \Gamma_0} = P_0 \mathbf{u}_{0, \Gamma_0}, \quad (76)$$

which is employed in Eqs. (17) and (18) (dropping Γ_0 from the notation).